Journal of Molecular Catalysis A: Chemical 417 (2016) 168–183

Contents lists available at ScienceDirect

Journal of Molecular Catalysis A: Chemical

journal homepage: www.elsevier.com/locate/molcata

Controlled hydrothermal synthesis of $PbBiO_2Br$/BiOBr heterojunction with enhanced visible-driven-light photocatalytic activities

Ho-Pan Lin [a], Wenlian William Lee [b,c], Shiuh-Tsuen Huang [a], Li-Wen Chen [a], Tsung-Wen Yeh [a], Jing-Ya Fu [a], Chiing-Chang Chen [a,*]

[a] Department of Science Education and Application, National Taichung University of Education, Taichung 403, Taiwan
[b] Department of Occupational Safety and Health, Chung-Shan Medical University, Taichung 402, Taiwan
[c] Department of Occupational Medicine, Chung-Shan Medical University Hospital, Taichung 402, Taiwan

ARTICLE INFO

Article history:
Received 15 January 2016
Received in revised form 6 March 2016
Accepted 8 March 2016
Available online 16 March 2016

Keywords:
$PbBiO_2Br$
BiOBr
heterojunction
photocatalytic
crystal violet

ABSTRACT

This is the first report that $PbBiO_2Br$/BiOBr is synthesized by a template-free hydrothermal method. The composition and morphologies of the samples could be controlled by adjusting some growth parameters, including reaction pH, Pb/Bi molar ratio, and temperature. All the samples are characterized by XRD, TEM, XPS, SEM-EDS, FT-IR, BET, EPR, and UV-vis-DRS. The $PbBiO_2Br$/BiOBr photocatalysts exhibit enhanced photocatalytic activities on the degradation of crystal violet (CV) under visible-light irradiation. In particular, the catalytic performance illustrates the best reaction rate constant 1.257×10^{-1} h^{-1} once $PbBiO_2Br$/BiOBr is used as the photocatalyst; which is 3 and 2 times higher than the reaction rate constant of $PbBiO_2Br$ and BiOBr being the photocatalysts, respectively. This study reveals that $PbBiO_2Br$/BiOBr can be used to suppress the recombination of photoinduced electron-hole pairs and contribute to the enhanced photocatalytic efficiency of semiconductors in the visible-light-driven catalysis. The possible photodegradation mechanism is studied by examining different active species through EPR and adding appropriate scavengers. The results demonstrate that the reactive O_2^- plays the major and OH the minor roles in the CV degradation.

1. Introduction

In face of an increasingly serious environmental pollutant and energy crunch, photocatalysis, as a suitable technology, plays an important role in the degradation of pollutants and solar energy conversion [1,2]. For the practical applications of photocatalysis, an environmentally powerful and cheap photocatalyst is an important component [3]. CV, a cationic triphenylmethane dye, was found the use as colorants in industry and as antimicrobial agents [4]. However, great troubles were arisen about the thyroid peroxidase-catalyzed oxidation of the triphenylmethane class of dyes because the reactions might produce various *N*-de-alkylated primary and secondary aromatic amines, with the structures similar to aromatic amine carcinogens [5]. Photocatalytic degradation of CV was studied using several systems that generated active species, including heterojunctions $SrFeO_{3-x}$/g-C_3N_4 [6], BiOX/BiOY(X, Y = Cl, Br, I) [7], etc. and pure semiconductors $Bi_xAg_yO_z$ [8], Bi_2WO_6 [9], TiO_2 [10], ZnO [11], $MTiO_3$ (M = Sr, Ba) [12,13], etc.

Over the past decades, a two-dimensional (2D) anisotropic nanostructure of a semiconductor material, which is of a nanoscale dimension in thickness only and infinite length in the plane, has attracted great research interests [14]. In such a unique anisotropic 2D structure, photoinitiated charge carriers experienced two kinds of limitation. The strong limitation (thickness) was necessary to sufficiently increase the free energy of the conduction band electrons for the photocatalytic degradation; meanwhile, the weak limitation (length and width) was needed to facilitate effective delocalization of longer-living excitons and separated charges. Thereby, the probability of photoinduced electron–hole recombination was effectively minimized. Thus, the exploration of facile and efficient methods for the synthesis of 2D nanomaterials might greatly improve their current performance and open up new applications [15,16].

Recently, Bi-based layered structure compounds, within Aurivillius family, such as BiOX (X = Cl, Br, I) [17,18], Bi_2WO_6 [19], $BiVO_4$ [20], $Bi_4Ti_3O_{12}$ [21], etc., have been extensively searched as highly efficient photocatalysts due to their unique layered structure and high catalytic activities. It is thought that the Bi 6s and O 2p levels

* Corresponding author.
E-mail addresses: ccchen@mail.ntcu.edu.tw, ccchen@ms3.ntcu.edu.tw (C.-C. Chen).

http://dx.doi.org/10.1016/j.molcata.2016.03.021
1381-1169/

can make a largely dispersed hybridized valence band, which favors the mobility of photogenerated holes and the oxidation reaction, inducing efficient separation of photogenerated electron-hole pairs and then improving the photocatalytic efficiency [22]. Many inorganic materials have modular structures, where individual units are responsible for different functions. The $[Bi_2O_2]^{2+}$ slabs with the α-PbO type structure as well as simple halide layers (Cl^- or Br^-) are effective spacers in some layered functional materials [23]. Previous reports discussed mainly electronic reasons for the different photocatalytic activities of layered $PbBiO_2X$-type materials (X = Cl, Br, I) [24–27]. However, crystal-chemical arguments should also be taken into consideration to explain the photocatalytic properties of the compounds. A possible reason for the different catalytic activities of the oxides may be derived collectively from their crystal structures, their optic, and their redox properties. All the solid materials under discussion crystallize in a layered structure. They exhibit covalent metal oxygen layers $[PbBiO_2]^+$ separated by halide layers, which are stacked along [001]. One can assume that the crystal surface consists of metal oxygen layers, i.e., the metal atoms are expected to form the (001) surfaces. In case of the bismuth compounds, the metal position was statistically occupied by lead and bismuth in the ratio 1:1 [28,29]. It was reported that the band gaps of $PbBiO_2Cl$ [25], $PbBiO_2Br$ [24], and $PbBiO_2I$ [26] were 2.53, 2.47, and 2.39 eV, respectively. It seemed that the gaps of all these semiconductors were in the visible-light range to catalyze the photocatalytic reaction.

Recently, the development of visible-light-driven photocatalyst has obtained considerable attention as an alternative in wastewater treatment. An effective and simple tactics to improve the photocatalytic activity of a photocatalyst is the incorporation of a heterostructure, because heterojunctions have great potential for tuning the wished electronic properties of photocatalysts and efficiently separating the photogenerated electron–hole pairs [30–32]. So far, a heterojunction concerned $PbBiO_2Br$, such as $PbBiO_2Br/NbSe_2$, has been reported and exhibited the enhanced photocatalytic efficiency [33]. Therefore, it is feasible for $PbBiO_2Br$ being partly transformed into $NbSe_2$ via a thermodynamically favored direction through the ion exchange reaction, which allows the exchange between the component ions and the incoming species [34], to consequently obtain the $PbBiO_2Br/NbSe_2$ heterojunction.

To the best of our knowledge, nanocomposite semiconductors consisting of $PbBiO_2Br$ and BiOBr have not yet been reported in the literature. This is the first report that $PbBiO_2Br$/BiOBr composites are prepared by a template-free hydrothermal method and characterized by FE-SEM-EDS, XRD, HR-XPS, and UV-vis-DRS. Through degrading CV in aqueous solution under visible-light irradiation, the photocatalytic activities of $PbBiO_2Br$/BiOBr composites are further discussed.

2. Experimental Details

2.1. Materials

$Pb(NO)_3{\bullet}H_2O$, ammonium oxalate (Osaka), CV dye (TCI), *p*-benzoquinone (Alfa aesar), $BiBr_3$, sodium azide (Sigma-Aldrich), and isopropanol (Merck) were purchased and used without further purification. Reagent-grade NaOH, HNO_3, CH_3COONH_4, and HPLC-grade methanol were obtained from Merck.

2.2. Instruments and analytical methods

The X-ray diffraction (XRD) patterns were recorded on a MAC Science MXP18 equipped with Cu-Kα radiation, operating at 40 kV and 80 mA. Field emission scanning electron microscopy-electron dispersive X-ray spectroscopy (FE-SEM-EDS) measurements were carried out using a JEOL JSM-7401F at an acceleration voltage 15 kV. The Al-Kα radiation was generated at 15 kV. The field-emission transmission electron microscopy (FE-TEM) images, selected area electron diffraction (SAED) patterns, high resolution transmission electron microscopy (HRTEM) images, and energy-dispersive X-ray spectra (EDS) were obtained using JEOL-2010 with an accelerating voltage of 200 kV. High resolution X-ray photoelectron spectroscopy (HRXPS) measurements were carried out using ULVAC-PHI. The Ultra-violet photoelectron spectroscopy (UPS) measurements were performed using ULVAC-PHI XPS, PHI Quantera SXM. The Brunauer-Emmett-Teller (BET) specific surface areas of the samples (S_{BET}) were measured with an automated system (Micrometrics Gemini) using nitrogen gas as the adsorbate at liquid nitrogen temperature. The mineralization of CV was monitored by measuring the total organic carbon (TOC) content with a Dohrmann Phoenix 8000Carbon Analyzer using a UV/persulfate oxidation method by directly injecting the aqueous solution into the instrument.

2.3. Synthesis of $PbBiO_2Br$/BiOBr

1, 3, 5 mmol $Pb(NO_3)_2{\bullet}H_2O$ and 3 mmol $BiBr_3$ were first mixed in a 50 mL flask, and followed by adding 30 mL H_2O. With continuous stirring, 2 M NaOH was added dropwise to adjust the pH = 1-14. The solution was then stirred vigorously for 30 min and 10 mL solution transferred into a 30 mL Teflon-lined autoclave, which was heated up to 100–250 °C for 12 h and then naturally cooled down to room temperature. These resulted solid precipitate was collected by filtration, washed with deionized water and methanol to remove any possible ionic species in the solid precipitate, and then dried at 60 °C overnight. Depending on the $Pb(NO_3)_2{\bullet}H_2O/BiBr_3$ molar ratio (1:3, 3:3, 5:3), pH value, temperature, and reaction times, the samples were synthesized and labeled as shown in Table 1; the as-prepared samples were labeled from P1B3-100-1-12 to P5B3-250-14-12

2.4. Photocatalytic experiments

The CV irradiation experiments were carried out on stirred aqueous solution contained in a 100-mL flask; the aqueous suspension of CV (100 mL, 10 ppm) and the amount of catalyst powder were placed in a Pyrex flask. The pH of the suspension was adjusted by adding either NaOH or HNO_3 solution. Dark experiments were performed in order to examine the adsorption/desorption equilibrium. 10 mg of the photocatalyst was mixed with 100 mL CV aqueous solution with a known initial concentration in a 100 mL flask and the mixture was shaken in an orbital shaker (100 rpm) at a constant temperature. The mixture was centrifuged at 3000 rpm in a centrifugation machine after batch sorption experiments so that the absorbance of CV could be determined at 580 nm by means of HPLC-PDA-ESI-MS. The concentrations of the solutions were determined using linear regression equation. Prior to the irradiation, the suspension was magnetically stirred in dark for ca. 30 min to establish an adsorption/desorption equilibrium between the CV and the catalyst surface. Irradiation was carried out using 150 W Xe arc lamps, the light intensity was fixed at 31.2 W/m^2, and the reaction vessel was placed 30 cm from the light source. At given irradiation time intervals, a 5-mL aliquot was collected and centrifuged to remove the catalyst. The supernatant was measured by HPLC-PDA-ESI-MS.

A different quencher was introduced to scavenge the relevant active species in order to evaluate the effect of the active species during the photocatalytic reaction. $O_2{\bullet}^-$, ${\bullet}OH$, h^+, and $^1O_2$ were studied by adding 1.0 mM benzoquinone (BQ, a quencher of $O_2{\bullet}^-$) [35], 1.0 mM isopropanol (IPA, a quencher of ${\bullet}OH$) [36], 1.0 mM ammonium oxalate (AO, a quencher of h^+) [37], and 1.0 mM sodium

Table 1
Codes of as-prepared samples under different hydrothermal conditions. ($Pb(NO_3)_2/BiBr_3$ = 1/3–5/3, pH = 1–14, temp = 100–250 °C, time = 12 h).

Temperature (°C)/	pH value					
Molar ratio (Pb:Bi)	1	4	7	10	13	14
100(1:3)	P1B3-100-1-12	P1B3-100-4-12	P1B3-100-7-12	P1B3-100-10-12	P1B3-100-13-12	P1B3-100-14-12
100(3:3)	P3B3-100-1-12	P3B3-100-4-12	P3B3-100-7-12	P3B3-100-10-12	P3B3-100-13-12	P3B3-100-14-12
100(5:3)	P5B3-100-1-12	P5B3-100-4-12	P5B3-100-7-12	P5B3-100-10-12	P5B3-100-13-12	P5B3-100-14-12
150(1:3)	P1B3-150-1-12	P1B3-150-4-12	P1B3-150-7-12	P1B3-150-10-12	P1B3-150-13-12	P1B3-150-14-12
150(3:3)	P3B3-150-1-12	P3B3-150-4-12	P3B3-150-7-12	P3B3-150-10-12	P3B3-150-13-12	P3B3-150-14-12
150(5:3)	P5B3-150-1-12	P5B3-150-4-12	P5B3-150-7-12	P5B3-150-10-12	P5B3-150-13-12	P5B3-150-14-12
200(1:3)	P1B3-200-1-12	P1B3-200-4-12	P1B3-200-7-12	P1B3-200-10-12	P1B3-200-13-12	P1B3-200-14-12
200(3:3)	P3B3-200-1-12	P3B3-200-4-12	P3B3-200-7-12	P3B3-200-10-12	P3B3-200-13-12	P3B3-200-14-12
200(5:3)	P5B3-200-1-12	P5B3-200-4-12	P5B3-200-7-12	P5B3-200-10-12	P5B3-200-13-12	P5B3-200-14-12
250(1:3)	P1B3-250-1-12	P1B3-250-4-12	P1B3-250-7-12	P1B3-250-10-12	P1B3-250-13-12	P1B3-250-14-12
250(3:3)	P3B3-250-1-12	P3B3-250-4-12	P3B3-250-7-12	P3B3-250-10-12	P3B3-250-13-12	P3B3-250-14-12
250(5:3)	P5B3-250-1-12	P5B3-250-4-12	P5B3-250-7-12	P5B3-250-10-12	P5B3-250-13-12	P5B3-250-14-12

azide (SA, a quencher of $^1O_2$ [38], respectively. The method was similar to the former photocatalytic activity test.

3. Results and Discussion

3.1. Characterization of as-prepared samples

3.1.1. XRD

Fig. 1 and Figs. S1-S3 show the XRD patterns of the as-prepared samples; the patterns clearly show the existence of the pure phase, $PbBiO_2Br$ and BiOBr, and the composites, $PbBiO_2Br$/BiOBr, Pb(OH)Br/BiOBr, $PbBiO_2Br$/Pb(OH)Br/BiOBr, $PbBiO_2Br$/Pb(OH)Br, $PbBiO_2Br/Bi_{12}O_{17}Br_2$, and $PbBiO_2Br/Bi_2O_3$. Table 2 summarizes the results of the XRD measurements. All the samples as-prepared contain BiOBr phase (JCPDS 78–0348), $PbBiO_2Br$ phase (JCPDS 38–1008), Pb(OH)Br phase (JCPDS 89–0624), $Bi_{12}O_{17}Br_2$ phase (JCPDS 37–0701), and Bi_2O_3 (JCPDS 71–0466).

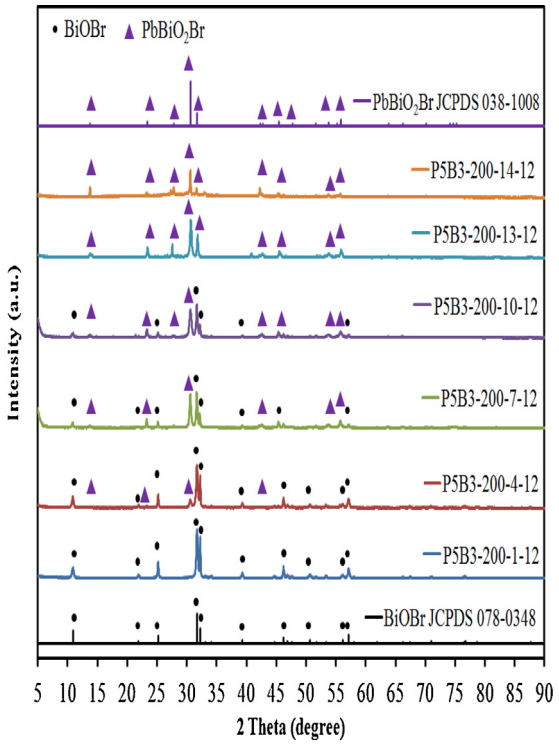

Fig. 1. XRD patterns of as-prepared samples under different pH values, at reaction temperature 200 °C and reaction times 12 h. (Molar ratio $Pb(NO_3)_2/BiBr_3$ = 5/3).

3.1.2. TEM

Fig. 2 displays that $PbBiO_2Br$/BiOBr, Pb(OH)Br/BiOBr, and $PbBiO_2Br$/Pb(OH)Br/BiOBr are composed of different-size layers, consistent with the TEM observations. In addition, the EDS spectrum shows that the sample contains the elements of Bi, Pb, Br, and O. In Fig. 2(a), the HRTEM image demonstrates that two sets of lattice images are obtained with d-spacings of 0.641 and 0.193 nm, corresponding to the (002) plane of $PbBiO_2Br$ and the (113) plane of BiOBr, the d-spacings of 0.226 and 0.353 nm corresponded to the (302) plane of Pb(OH)Br and the (101) plane of BiOBr (Fig. 2(b)), and the d-spacings of 0.291, 0.211, and 0.281 nm corresponded to the (103) plane of $PbBiO_2Br$, the (213) plane of Pb(OH)Br, and the (102) plane of BiOBr (Fig. 2(c)), respectively, which is in strong agreement with the XRD results. The results suggest that the $PbBiO_2Br$/BiOBr, $PbBiO_2Br$/Pb(OH)Br/BiOBr, Pb(OH)Br/BiOBr phases have been formed in the composites, which are favorable for the separation of photoinduced carriers, yielding high photocatalytic activities.

3.1.3. XPS

Fig. 3 presents the Bi 4f, Br 3d, Pb 4f, and O 1s XPS spectra of the $PbBiO_2Br$/BiOBr composites. Observation of the transition peaks involving the Bi 4f, Br 3d, Pb 4f, and O 1s orbitals identifies that the catalysts are composed of Bi, Br, Pb, and O. The characteristic binding energy value 158.1 eV for Bi $4f_{7/2}$ (Fig. 3(a)) shows a trivalent oxidation state for bismuth. An additional spin–orbit doublet with the binding energy of 155.7 eV for Bi $4f_{7/2}$ also reveals in all samples, suggesting that certain parts of bismuth exist in the (+3-x) valence state. This shows that the trivalent bismuth partially reduces to the lower valence state by the hydrothermal method. A similar chemical shift of approximately 2.4 eV for Bi $4f_{7/2}$ was also published by Liao et al. [39]. They summarized that the Bi $^{(+3-x)}$ formal oxidation state could most probably be ascribed to the substoichiometric forms of Bi within the Bi_2O_2 layer, and the formation of the low oxidation state resulted in oxygen vacancy in the crystal lattice. However, it is supposed in this study that the Bi $^{(+3-x)}$ formal oxidation state could most likely be ascribed to the substoichiometric forms of Bi at the outer site of the particles, and the formation of the low oxidation state results in oxygen vacancy in the crystal surface, revealing that the main chemical states of the bismuth element in the samples are not trivalent.

From Fig. 3(c), the binding energy 136.4 and 137.2 eV is attributed to Pb $4f_{7/2}$ respectively, which could be pointed to Pb at the divalent oxidation state [40]. Kovalev et al. demonstrated

Table 2
Crystalline phase changes of as-prepared samples under different hydrothermal conditions. ($Pb(NO_3)_2/BiBr_3$ = 1/3–5/3, pH = 1–14, temp = 100–250 °C, time = 12 h). ● BiOBr; ◆ $Bi_{12}O_{17}Br_2$; ■ Pb(OH)Br; ▲ PbBiO2Br; ○ Bi_2O_3.

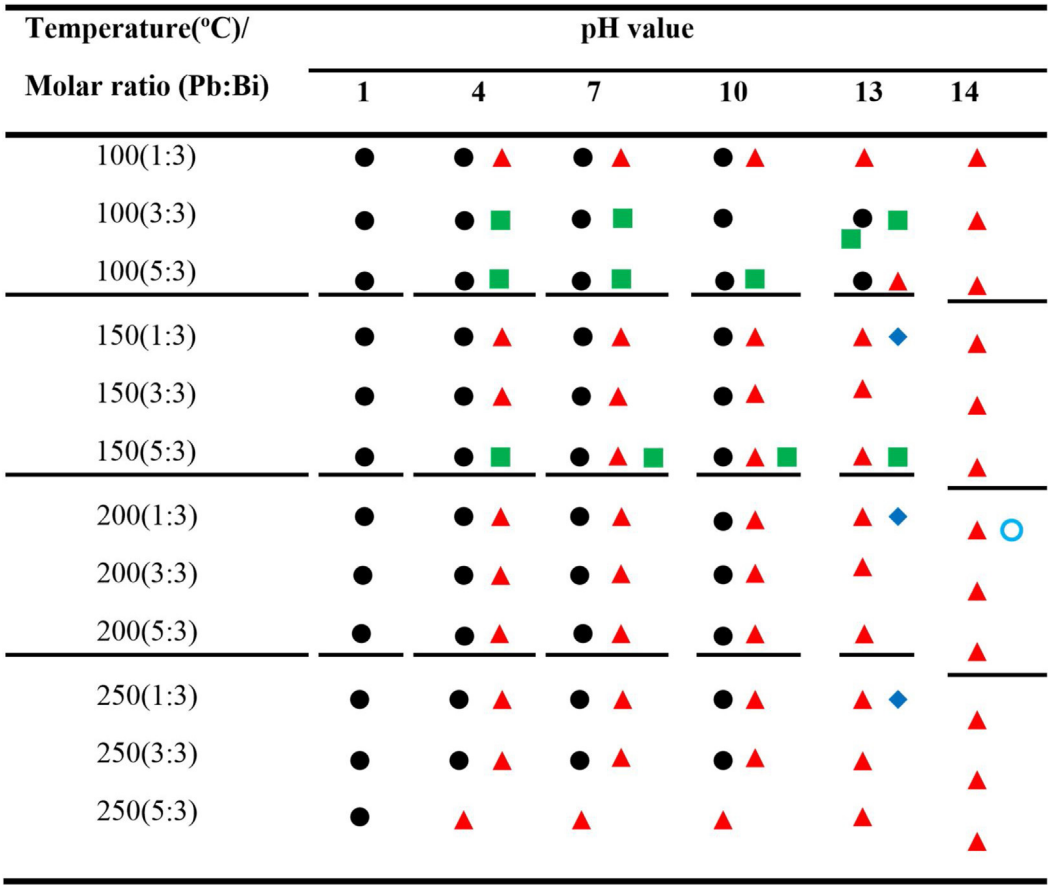

that the particle size of PbS could be correlated with observable changes in the binding energy of the Pb XPS peak. They reported that relative integral intensity of the peak depended upon the fraction of particle in the specific region [41,42], which indicated that higher successive ionic layer adsorption and reaction cycle led to the formation of the fraction of bigger and smaller particles on the surface of titania nanotube. The $4f_{5/2}$ peak observed at 137.8 and 138.9 eV is due to the presence of two different particle sizes of PbS formed in TiO_2 nanotube arrays. The asymmetric O 1s peak shown in Fig. 3(d) can be split by using the XPS peak-fitting program. The peak at 530.4 eV is assigned to the external –OH group or the water molecule adsorbed on the surface, and the other O 1s peak appearing at 528.8 eV corresponds to lattice oxygen atoms in $PbBiO_2Br$/BiOBr [43]. These results agree with those of XRD and TEM experiment.

According to earlier studies [39,44,45], a series of bismuth oxybromides in the formation process were reported by Chen et al. The proposed processes for the formation of $PbBiO_2Br$/BiOBr, $PbBiO_2Br$/Pb(OH)Br/BiOBr, Pb(OH)Br/BiOBr composites are described in equations 1–8. The results demonstrate a series of changes in the compounds prepared at different hydrothermal conditions, described as $BiOBr \rightarrow Bi_4O_5Br_2 \rightarrow Bi_{24}O_{31}Br_{10} \rightarrow Bi_3O_4Br \rightarrow Bi_5O_7Br \rightarrow Bi_{12}O_{17}Br_2 \rightarrow Bi_2O_3$ and $PbBr_2 \rightarrow Pb(OH)Br \rightarrow PbBiO_2Br$. By controlling the pH of the hydrothermal reaction, different compositions are obtained as follows.

$$Bi^{3+} + 3OH^- \rightarrow Bi(OH)_{3(s)} \quad (1)$$

$$2Bi(OH)_{3(s)} + Br^- \rightarrow BiOBr_{(s)} + H_2O + OH^- \quad (2)$$

$$Bi^{3+} + 3Br^- \rightarrow BiBr_{3(s)} \quad (3)$$

$$BiBr_{3(s)} + 2OH^- \rightarrow BiOBr_{(s)} + 2Br^- + H_2O \quad (4)$$

$$Pb^{2+} + 3Br^- \rightarrow PbBr_{2(s)} \quad (5)$$

$$PbBr_{2(s)} + OH^- \rightarrow Pb(OH)Br_{(s)} \quad (6)$$

$$Pb(OH)Br_{(s)} + 2OH^- \rightarrow Pb(OH)_2 \quad (7)$$

$$BiOBr_{(s)} + Pb(OH)_2 \rightarrow PbBiO_2Br_{(s)} + H_2O \quad (8)$$

3.1.4. Morphological structure and composition

Fig. 4 and Figs. S4-S14 show the FESEM images of the pure BiOBr, $PbBiO_2Br$ and the composites $PbBiO_2Br$/BiOBr, $PbBiO_2Br/Bi_{12}O_{17}Br_2$, Pb(OH)Br/BiOBr, $PbBiO_2Br$/Pb(OH)Br/BiOBr, $PbBiO_2Br$/Pb(OH)Br, $PbBiO_2Br/Bi_2O_3$ at high magnification, respectively. From the observations, $PbBiO_2Br$, Pb(OH)Br, $Bi_{12}O_{17}Br_2$, $Bi_{12}O_{17}Br_2$ samples show square-plate, rod, nano-thin-sheet (or flower-like), and irregular-nanosheet morphology, respectively. The SEM-EDS results demonstrate that the main elements within these samples are lead, bismuth, oxygen, and bromine at Table 3 and S1-S2. From above results, the pure phase $PbBiO_2Br$, BiOBr and the composites $PbBiO_2Br$/BiOBr could be selectively synthesized through a controlled hydrothermal method.

3.1.5. Optical absorption properties

As shown in Fig. 5 and Figs. S15-S16 for DR-UV of the as-prepared samples, the absorption edge of the pure phase $PbBiO_2Br$ (or BiOBr) is around 500.0–529.9 (or 435.1–442.9) nm, which originates from its band gap of 2.34–2.48 (or 2.80–2.85) eV (Table 4

and S3-S4) and is consistent with the reported results [24,39]. Pure $PbBiO_2Br$ and BiOBr absorb only a small amount of visible light. The E_g value of $PbBiO_2Br$/BiOBr is determined from a plot of $(\alpha h\nu)^{1/2}$ vs energy ($h\nu$), which is calculated as 2.39–2.72 eV.

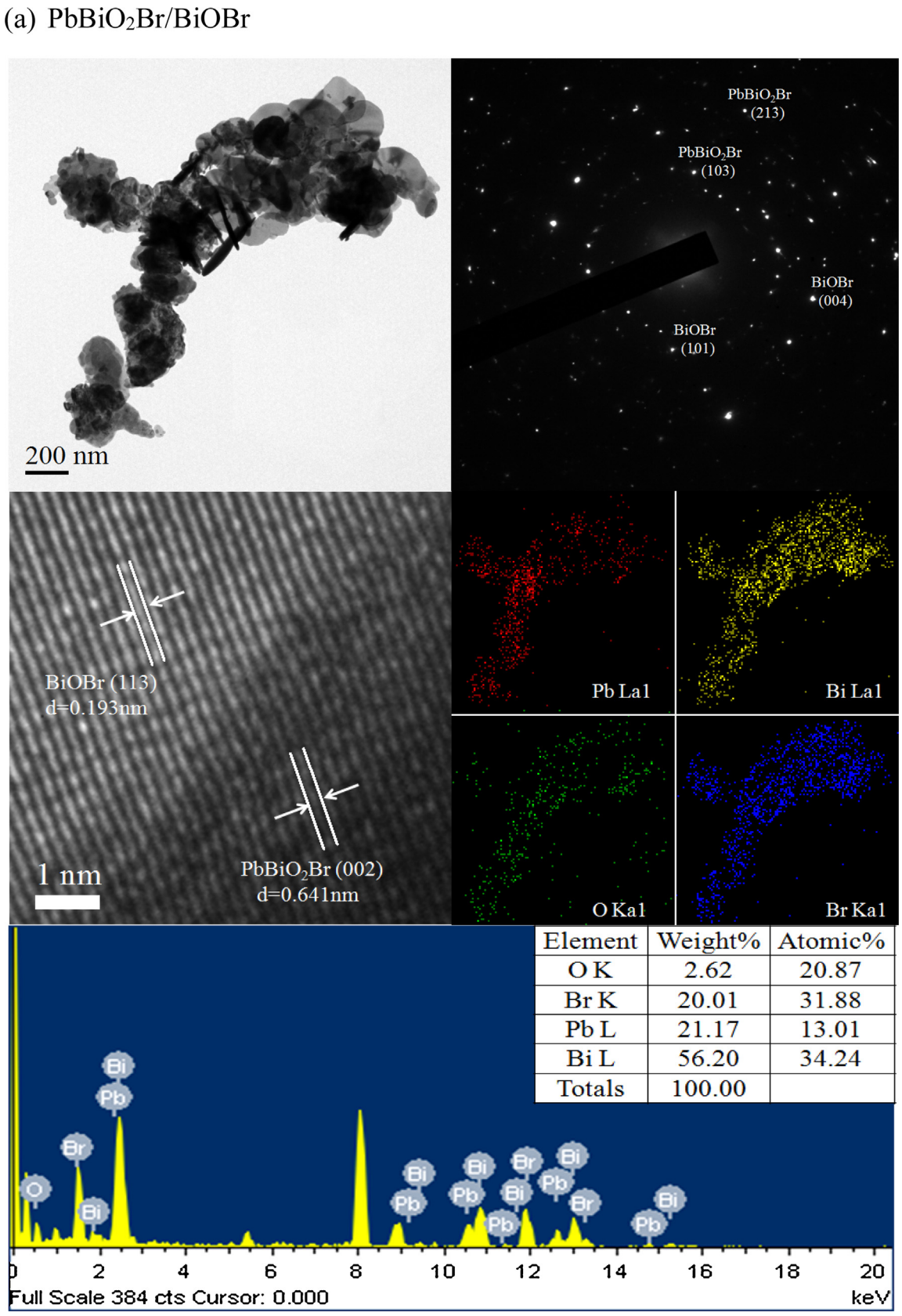

Fig. 2. FE-TEM images, SAD, mapping, and EDS of (a) P5B3-200-10-12, (b) P5B3-150-4-12, and (c) P5B3-150-7-12 samples by the hydrothermal autoclave method.

(b) Pb(OH)Br/BiOBr

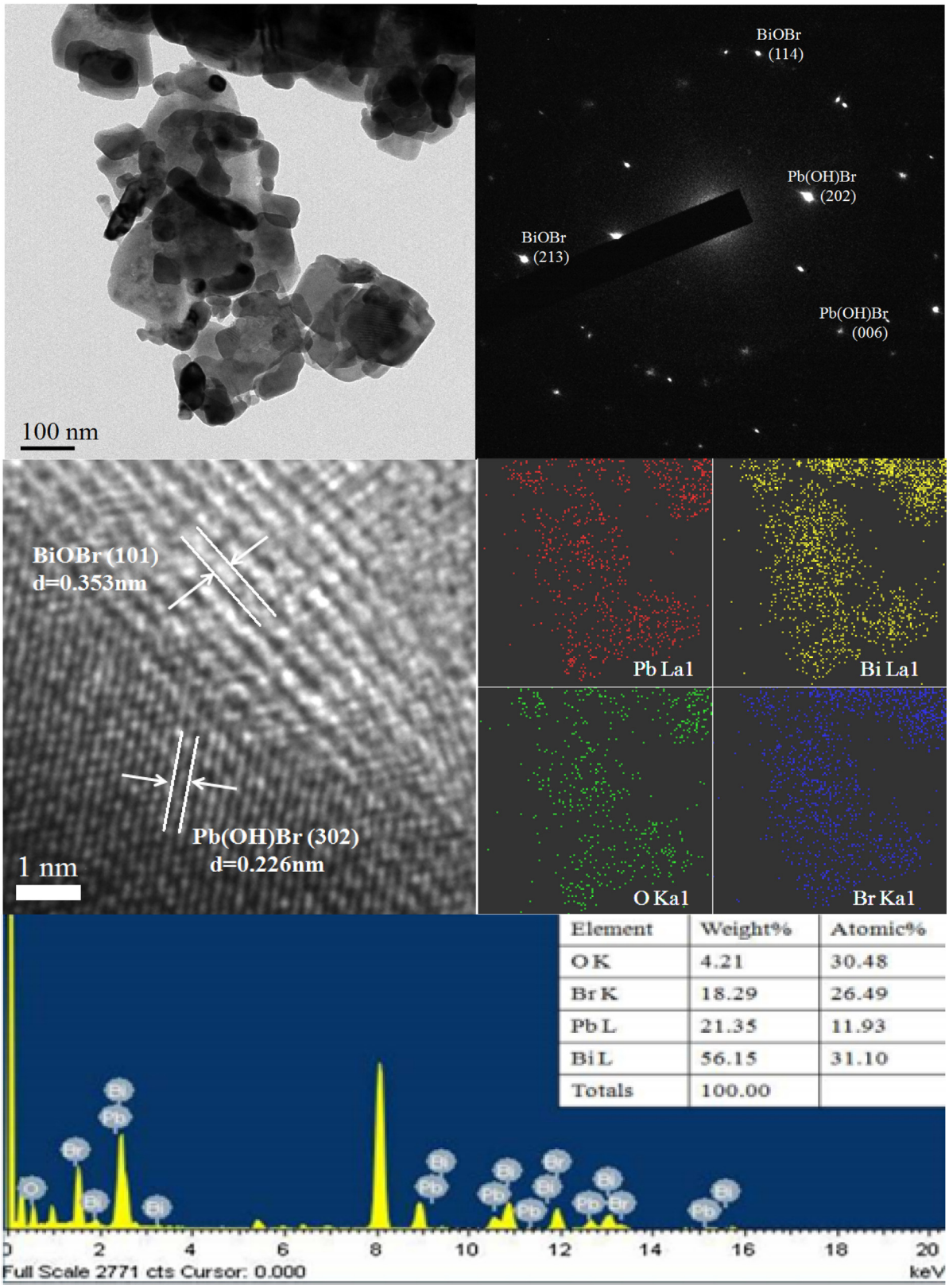

Element	Weight%	Atomic%
O K	4.21	30.48
Br K	18.29	26.49
Pb L	21.35	11.93
Bi L	56.15	31.10
Totals	100.00	

Fig. 2. (*Continued*).

(c) PbBiO2Br/Pb(OH)Br/BiOBr

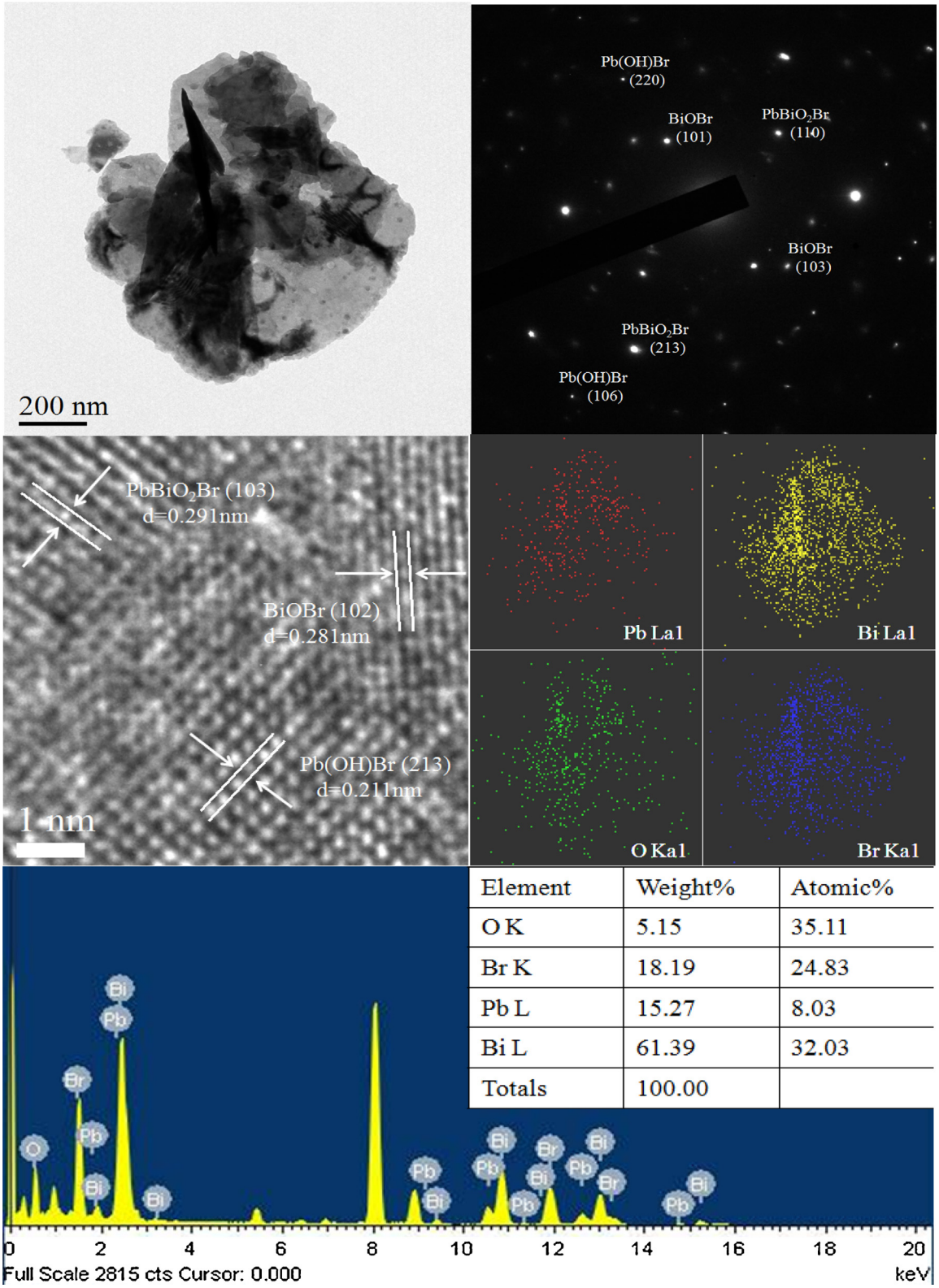

Element	Weight%	Atomic%
O K	5.15	35.11
Br K	18.19	24.83
Pb L	15.27	8.03
Bi L	61.39	32.03
Totals	100.00	

Fig. 2. (*Continued*).

3.1.6. BET and Adsorption-desorption isotherm

From Table 4 and S3-S4, the $PbBiO_2Br$/BiOBr samples have S_{BET} around 6.60–15.85 m^2/g. However, the results of Table 4 and S3-S4 show that the P5B3-200-10-12 ($PbBiO_2Br$/BiOBr) sample—which shows the middle S_{BET}—does represent the highest photocatalytic activity ($k = 6.01 \times 10^{-2}\ h^{-1}$) among the samples, suggesting

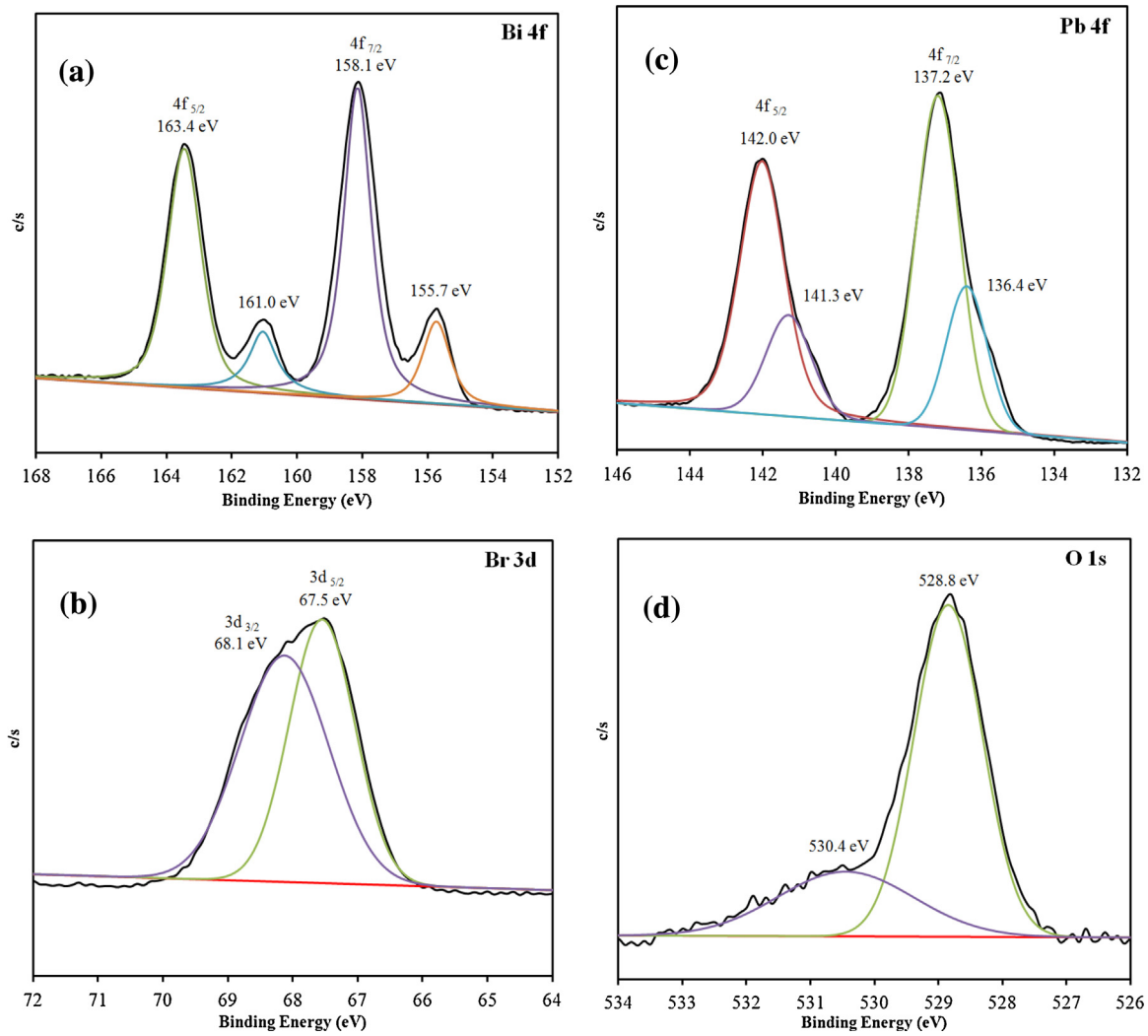

Fig. 3. High resolution XPS spectra of as-prepared P5B3-200-10-12 ($PbBiO_2Br$/BiOBr) samples. (a) Bi 4f; (b) Br 3d; (c) Pb 4f; (d) O 1s.

that the changes in the photocatalytic activity are resulted from $PbBiO_2Br$/BiOBr composites.

Fig. 6(a) shows the nitrogen adsorption-desorption isotherm curves of $PbBiO_2Br$/BiOBr, $PbBiO_2Br$, and BiOBr. The isotherms of $PbBiO_2Br$/BiOBr, $PbBiO_2Br$, and BiOBr are close to Type VI with a hysteresis loop at a highly relative pressure between 0.6 and 1.0 [46]. The shape of the hysteresis loop is close to Type H3, suggesting the existence of slit-like pores generally being formed by the aggregation of plate-like particles, which is consistent with the self-assembled nanoplate-like or nanosheet-like morphology of samples. This result is consistent with the image results of FE-SEM and TEM, showing that self-assembled nanosheets or nanoplates or nanosheets result in the formation of hierarchical architectures. Fig. 6(b) shows the corresponding pore-size distribution (PSD) of $PbBiO_2Br$/BiOBr and $PbBiO_2Br$ samples. The PSD curves are di-modal for the samples, indicating medium mesopores (10–30 nm) and large macropores (100–2000 nm). Because the nanosheets do not contain pores (Figs. 2 and 4), the medium mesopores may reflect porosity within nanosheets. The large macropores may attribute to the pores formed between stacked nanosheets, while the large macropores may be ascribed to the pores formed between nanosheets. Such self-organized porous architectures may be extremely useful in photocatalysis because they provide efficient transport pathways for reactant and product molecules [47]. The pore parameters of the as-prepared samples are summarized in Table 4 and S3-S4. The pore volume and size of the $PbBiO_2Br$/BiOBr composite sample were determined as the pore volume 0.084–0.2284 cm^3/g and 45.84–69.47 nm, respectively, compared to those of pure $PbBiO_2Br$ (0.0346–0.1886 cm^3/g and 46.34–64.30 nm) and BiOBr (0.0346–0.2218 cm^3/g and 47.15–70.33 nm).

3.2. Photocatalytic Activity

The changes in the UV–vis spectra during the photodegradation of CV in aqueous dispersions of $PbBiO_2Br$/BiOBr under visible light irradiation are illustrated in Fig. 7(a). After visible light irradiation for 12 h, approximately 80.5% of CV is decomposed. During visible light irradiation, the characteristic absorption band of the CV dye at approximately 588.5 nm decreases rapidly with slightly hypsochromic shifts (555.2 nm); however, no new absorption band appears even in the ultraviolet range ($\lambda > 200$ nm), indicating the possible formation of a series of *N*-demethylated intermediates and the possible cleavage of the whole conjugated chromophore structure of the CV dye. Further irradiation causes the absorption band at 555.2 nm to decrease; however, no further wavelength shift is observed, suggesting that the band at 555.2 nm is that of the full *N*-demethylated product of the CV dye [6,7].

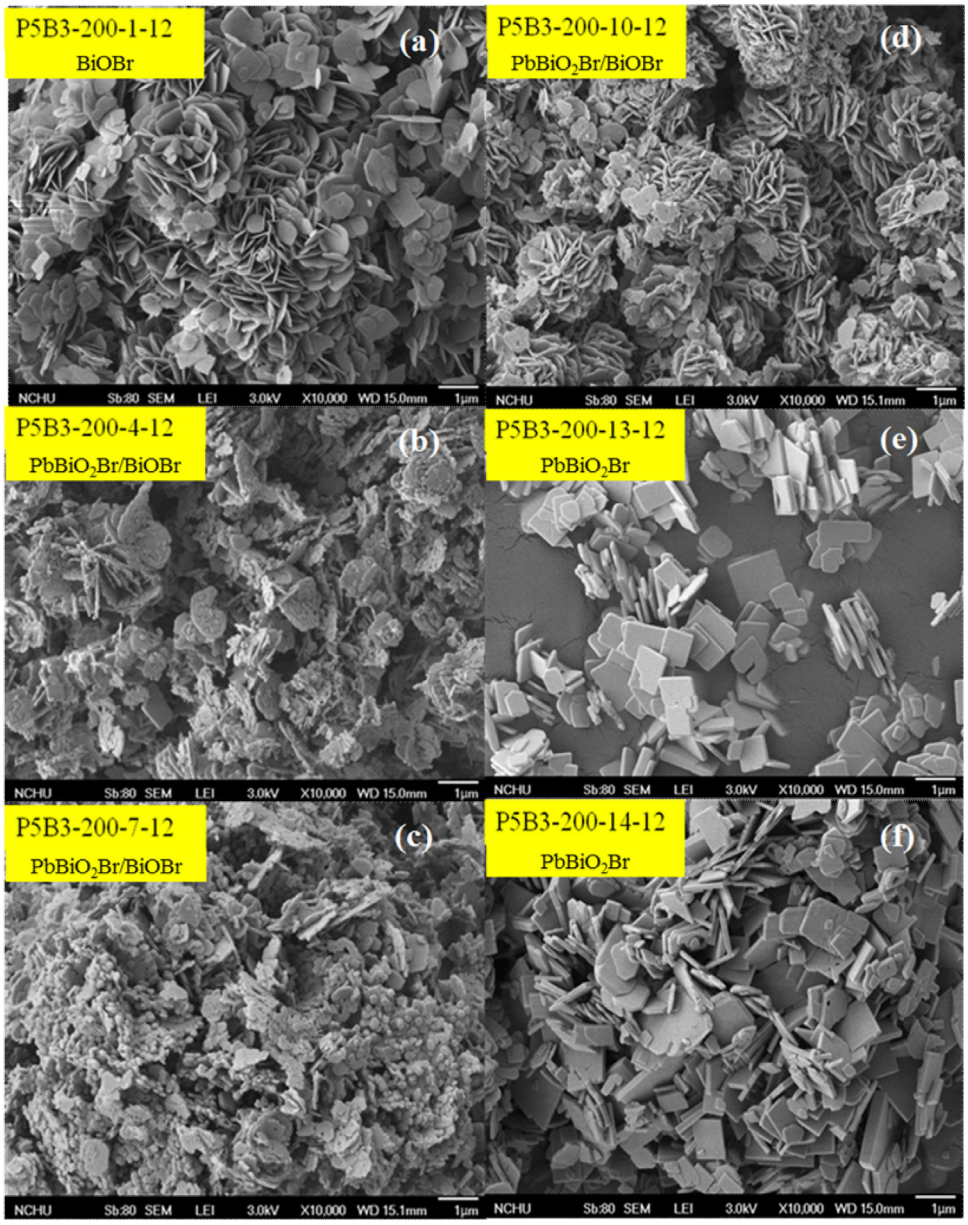

Fig. 4. SEM images of as-prepared samples by the hydrothermal autoclave method at different pH values. (Molar ratio $Pb(NO_3)_2/BiBr_3 = 5/3$, hydrothermal conditions: pH = 1–14, temp = 200 °C, time = 12 h).

The complete degradation of an organic molecule by photocatalysis normally leads to the conversion of all its carbon atoms to gaseous CO_2 and of the heteroatoms into inorganic anions that remain in solution. To study the total mineralization of CV, the total organic carbon (TOC) was determined as a function of irradiation time. Fig. 7(b) shows the decrease in the TOC percentage of CV during the photocatalytic degradation. The complete removal of 10 mg/L of CV was achieved after 96 h of treatment, and the corresponding carbon mineralization was 43%. The treatment was prolonged to 144 h to test whether the mineralization could be completed as well. Approximate 91% of CV was mineralized within 144 h of photocatalytic reaction time. Complete mineralization of CV was not achieved after 144 h of oxidation although CV disappeared after 96 h. This significant difference between degradation efficiency and mineralization efficiency implies that the products of CV oxidation mostly stayed at the intermediate product stage under the present experimental conditions.

The degradation efficiency as a function of reaction time is illustrated in Fig. 8 and Figs. S17-S19; the removal efficiency is significantly enhanced in the presence of the as-prepared samples. After the irradiation for 72 h, P5B3-200-10-12 ($PbBiO_2Br$/BiOBr) exhibits a superior photocatalytic performance, with the CV removal efficiency up to 98%. To further understand the reaction kinetics of CV degradation, the apparent pseudo-first-order model [48] expressed by $\ln(C_o/C) = kt$ equation is applied in the experiments. Via the first-order linear fit of the data shown in Table 4 and Table S3-S4, the k value of P5B3-200-10-12 ($PbBiO_2Br$/BiOBr) is obtained as the maximum degradation rate of $1.257 \times 10^{-1}\ h^{-1}$ using the first-order linear fit of the data, which is much higher than that of the other composites; the $PbBiO_2Br$/BiOBr (P5B3-200-10-12) composite is a much more effective photocatalyst than the others synthesized in this study. The photocatalytic activity of the $PbBiO_2Br$/BiOBr heterojunctons reaches the maximum rate constant $1.257 \times 10^{-1}\ h^{-1}$, 3 times higher than that of $PbBiO_2Br$

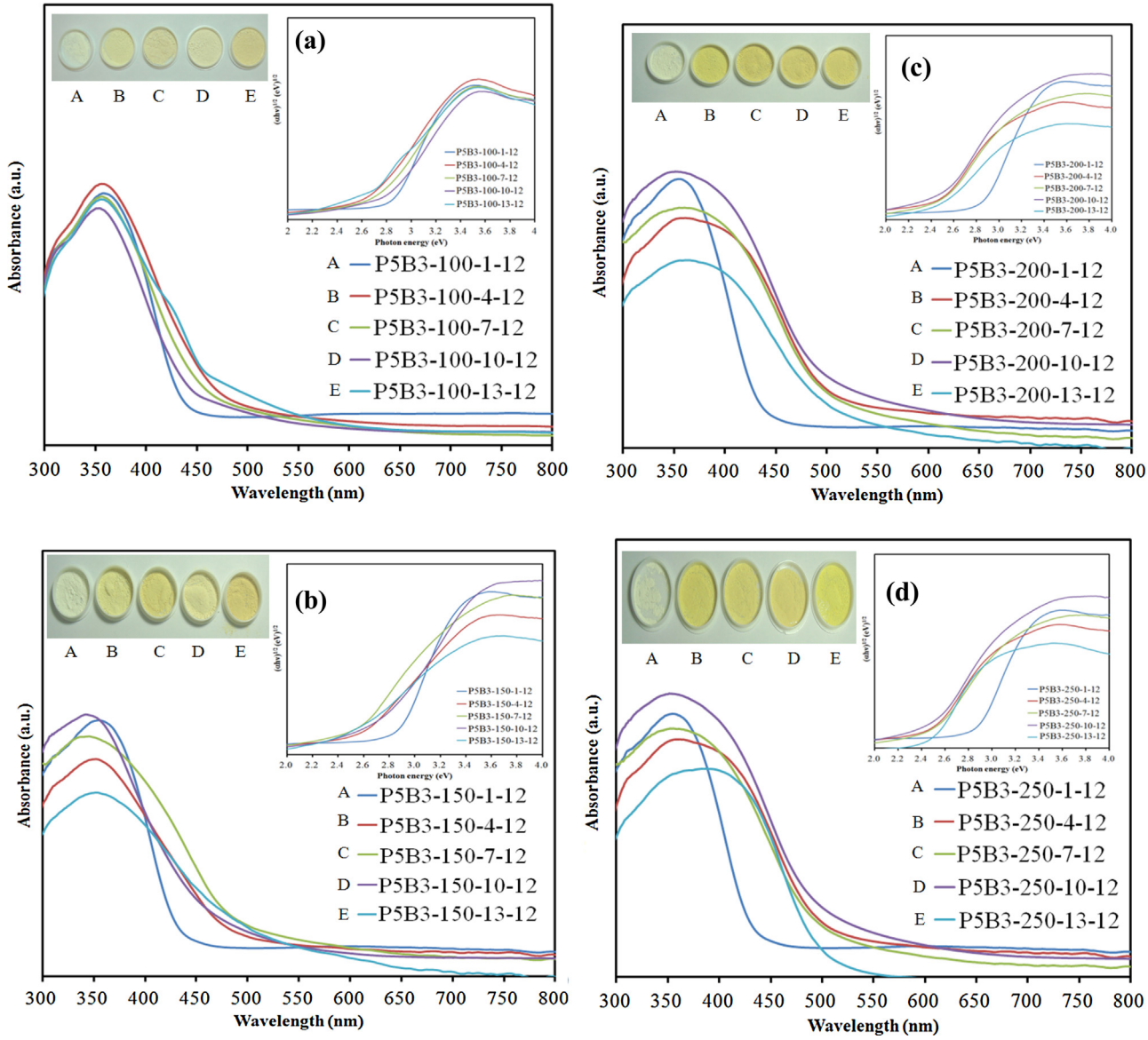

Fig. 5. UV–vis absorption spectra of the as-prepared photocatalysts under different pH values and reaction temperature. (Molar ratio $Pb(NO_3)_2/BiBr_3$ = 5/3, reaction time 12 h).

(P3B3-200-13-12) and 2 times higher than that of BiOBr (P1B3-200-1-12). Thus, the $PbBiO_2Br$/BiOBr heterojunctons may also play a role in enhancing the photocatalytic activity.

The durability of $PbBiO_2Br$/BiOBr is evaluated by recycling the used catalyst. After each cycle, the catalyst is collected by centrifugation. No apparent loss is observed in the photocatalytic activity when CV is removed in the 3rd cycle; even during the sixth run, the decline in the photocatalytic activity is 4.5% (Fig. 9(a)). The used $PbBiO_2Br$/BiOBr is also examined by XRD, and no detectable difference is observed between the as-prepared and the used samples (Fig. 9(b)); hence, $PbBiO_2Br$/BiOBr has good photostability.

3.3. Photodegradation Mechanism of CV

In general, three possible reaction pathways are assumed to be involved in the photodegradation of organic compounds by a photocatalyst, including (i) photocatalysis, (ii) photolysis, and (iii) dye photosensitization [49]. In the photolysis process, a photoinduced electron on the induced organism directly reacts with O_2 to produce a $^1O_2$ that acts as an oxidant for the photolysis of organism [50]. In the experiments, CV degradation induced by photolysis under visible light in a blank experiment is not observable, CV is a structure-stable dye, and the decomposition by the photolysis mechanism is negligible.

As people may know, various primary active species, such as HO, h^+, $O_2^{-\bullet}$, H and $^1O_2$, could be generated during the photocatalytic degradation reaction in UV-vis/semiconductor systems [50,51]. Dimitrijevic et al. [51] proposed that the water, both dissociated on the surface of TiO_2 and in subsequent molecular layers, had a three-fold role of (i) the stabilization of charges, preventing electron-hole recombination, (ii) an electron acceptor, the formation of H atoms in a reaction of photo-generated electrons with protons on the surface, $-OH_2^+$, and (iii) an electron donor, the reaction of water with photo-generated holes to give OH radicals. Ma et al. revealed that $O_2^{-\bullet}$ was the main active species for NO oxidation to NO_3^- with TO_2/g-C_3N_4 under visible and UV light [52]. Zou's group illustrated a typical Cu_2O–reduced graphene oxide photocatalyst being favorable for the production of $O_2^{-\bullet}$ reactive

Table 3
EDS of as-prepared samples prepared under different reaction conditions. ($Pb(NO_3)_2/BiBr_3$ = 5/3, pH = 1–14, temp = 100–250 °C, time = 12 h).

Sample code	EDS of atomic ratio (%)			
	Pb	Bi	O	Br
P5B3-100-1-12	–	30.40	42.35	27.24
P5B3-100-4-12	3.31	24.01	46.83	25.85
P5B3-100-7-12	2.81	24.71	49.28	23.20
P5B3-100-10-12	6.24	21.86	46.09	25.81
P5B3-100-13-12	13.08	23.82	58.97	14.53
P5B3-100-14-12	15.08	16.74	53.76	14.42
P5B3-150-1-12	–	30.22	44.01	25.77
P5B3-150-4-12	14.04	16.65	45.44	23.88
P5B3-150-7-12	14.78	16.45	52.75	16.01
P5B3-150-10-12	11.52	19.43	50.33	18.71
P5B3-150-13-12	12.09	19.41	55.57	12.93
P5B3-150-14-12	13.64	21.73	46.51	18.12
P5B3-200-1-12	–	30.77	44.09	25.14
P5B3-200-4-12	21.50	22.37	34.36	21.77
P5B3-200-7-12	15.30	17.28	50.85	16.57
P5B3-200-10-12	24.06	21.12	37.70	17.12
P5B3-200-13-12	24.06	21.12	37.70	17.12
P5B3-200-14-12	22.74	15.88	44.06	17.33
P5B3-250-1-12	–	30.39	41.63	27.97
P5B3-250-4-12	17.55	12.08	55.68	14.68
P5B3-250-7-12	11.11	20.22	50.71	17.96
P5B3-250-10-12	17.11	15.16	50.45	17.29
P5B3-250-13-12	21.13	22.18	37.45	19.24
P5B3-250-14-12	4.75	29.25	60.28	5.71

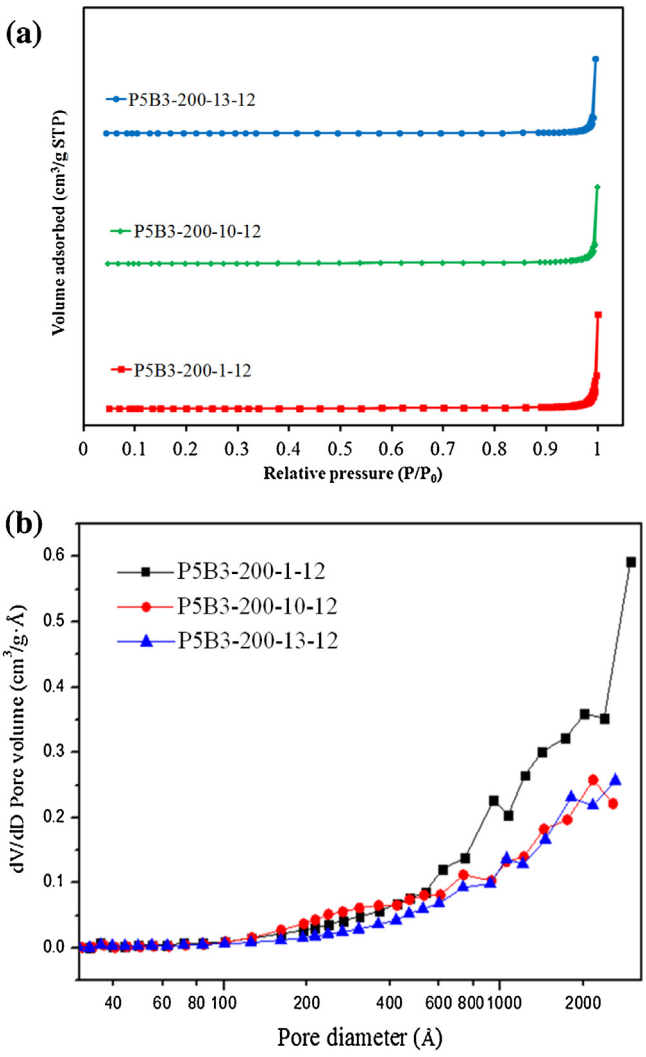

Fig. 6. (a) N_2 adsorption–desorption isotherm distribution curves and (b) the pore distribution curves for as-prepared samples under different pH values. (Molar ratio $Pb(NO_3)_2/BiBr_3$ = 5/3, hydrothermal conditions: pH = 1–14, temp = 200 °C, time = 12 h).

species for methylene blue [53]. Jiang et al. revealed that the photogenerated h^+ and $O_2^{-\bullet}$ were the main oxidative species for the degradation of methyl orange [54]. The generation of $O_2^{-\bullet}$ could not only inhibit the recombination of photoinduced charge carriers but also benefit the de-chlorination of chlorinated phenol derivative. The hydroxyl radical HO might only be formatted via an $e^- \rightarrow O_2^{-\bullet} \rightarrow H_2O_2 \rightarrow {}^\bullet OH$ route. Meanwhile, •OH radicals were formatted by multistep $O_2^{-\bullet}$ reduction in the system [55]. Kondrakov et al. reported the study on the photocatalytic generation of free OH radicals ($^\bullet OH_{free}$) in aqueous TiO_2 suspensions using an ^{18}O isotope labeling and a "remote" photocatalysis approach. A probe compound, 1,3,5-trichlorobenzene (TCB), was adsorbed in pores of silica gel (SG) microparticles to be shielded from the direct hole oxidation [56]. According to earlier studies [53], the photocatalytic process was mainly governed by $O_2^{-\bullet}$, rather than by •OH, e^- or h^+. In earlier study, CV photodegradation by BiO_mX_n/BiO_pX_q (X, Y = Cl, Br, I) under visible light was dominated by $O_2^{-\bullet}$ oxidation being the main active species and •OH and h^+ being the minor active species [55,57]. On the basis of the references presented above, it is proposed that the probability of forming •OH should be much lower than that for $O_2^{-\bullet}$; however, •OH is an extremely strong and nonselective oxidant, which leads to the partial or complete mineralization of several organic chemicals.

In order to evaluate the effect of the active species during the photocatalytic reaction, EPR measurement is used for scavenging the relevant active species. From Fig. 10, not only are the four characteristic peaks of DMPO-•OH adducts (1:2:2:1 quartet pattern) observed, but the six characteristic peaks of the DMPO-$O_2^{-\bullet}$ adducts are also observed under visible light irradiated $PbBiO_2Br$/BiOBr suspension. Fig. 10**(a)(b)** shows that no EPR signal is observed when the reaction is performed in the dark, while the signals with intensity corresponding to the characteristic peak of DMPO-•OH and DMPO-$O_2^{-\bullet}$ adducts [58] are observed during the reaction process under visible light irradiation, and the intensity gradually increases with the prolonged reaction time, suggesting that O_2^- and •OH being active species are formed in the presence of $PbBiO_2Br$/BiOBr and oxygen under visible light irradiation.

In order to re-evaluate the effect of the active species during the photocatalytic reaction, different quenchers are used for scavenging the relevant active species. As shown in Fig. 11, the photocatalytic degradation of CV is slightly affected by the addition of SA and AO, while the degradation efficiency of BQ and IPA quenching decreases evidently compared with that of no-quenching, indicating that $^1O_2$ and h^+ are the minor active species, whereas $O_2^{\bullet-}$ and •OH are the major active species in the mechanism of photocatalytic degradation of CV. Hence, the quenching effects of scavengers and EPR illustrate that the reactive O_2^- plays the major and OH plays the minor role in the photocatalytic degradation of CV. (Fig.12)

The structure characterizations have proven that $PbBiO_2Br$/BiOBr is a two-phase heterojunction. Considering that the heterojunction presents much higher photocatalytic activities than the component phase alone, it is reasonable that there might be synergetic effect between $PbBiO_2Br$ and BiOBr. Actually, many researchers have noted the synergetic effect in heterojunction systems consisting of two semiconductors in contact [59,60] and attributed the effect to the efficient charge transfer at the interface of two semiconductors, which would result in

Table 4
Physical and chemical properties of as-prepared samples at different conditions ($Pb(NO_3)_2/BiBr_3$ = 5/3, pH = 1–14, temp = 100–250 °C, time = 12 h) and the pseudo-first-order rate constants for the degradation of CV with photocatalysts under visible light irradiation.

Photocatalysts	S_{BET} (m^2/g)	Pore volume (cm^3/g)	Pore diameter (nm)	Band gap (eV)	k(h^{-1})	R^2
P5B3-100-1-12	8.75	0.1683	70.33	2.81	0.0276	0.9505
P5B3-100-4-12	4.47	0.0558	51.99	2.60	0.0128	0.9512
P5B3-100-7-12	4.40	0.0552	46.75	2.67	0.0171	0.9584
P5B3-100-10-12	5.13	0.0652	54.38	2.74	0.0232	0.9567
P5B3-100-13-12	5.56	0.0827	66.92	2.53	0.0090	0.9502
P5B3-150-1-12	10.33	0.2052	67.24	2.83	0.0453	0.9744
P5B3-150-4-12	4.78	0.0948	73.51	2.48	0.0416	0.9961
P5B3-150-7-12	6.58	0.0950	49.59	2.44	0.0159	0.9534
P5B3-150-10-12	8.33	0.1245	53.99	2.64	0.0160	0.9518
P5B3-150-13-12	5.51	0.1099	71.07	2.37	0.0097	0.9655
P5B3-200-1-12	11.82	0.2218	63.13	2.80	0.0207	0.9560
P5B3-200-4-12	6.97	0.1205	64.19	2.42	0.0281	0.9505
P5B3-200-7-12	8.50	0.1254	51.00	2.39	0.0253	0.9566
P5B3-200-10-12	9.55	0.1505	55.89	2.42	0.1257	0.9781
P5B3-200-13-12	8.09	0.1332	63.01	2.40	0.0017	0.9667
P5B3-250-1-12	3.51	0.0346	47.15	2.83	0.0413	0.9632
P5B3-250-4-12	7.00	0.1252	62.43	2.41	0.0278	0.9593
P5B3-250-7-12	8.04	0.1027	46.34	2.45	0.0258	0.9824
P5B3-250-10-12	7.96	0.1583	67.98	2.41	0.0333	0.9570
P5B3-250-13-12	3.51	0.0346	47.15	2.48	0.0029	0.9534

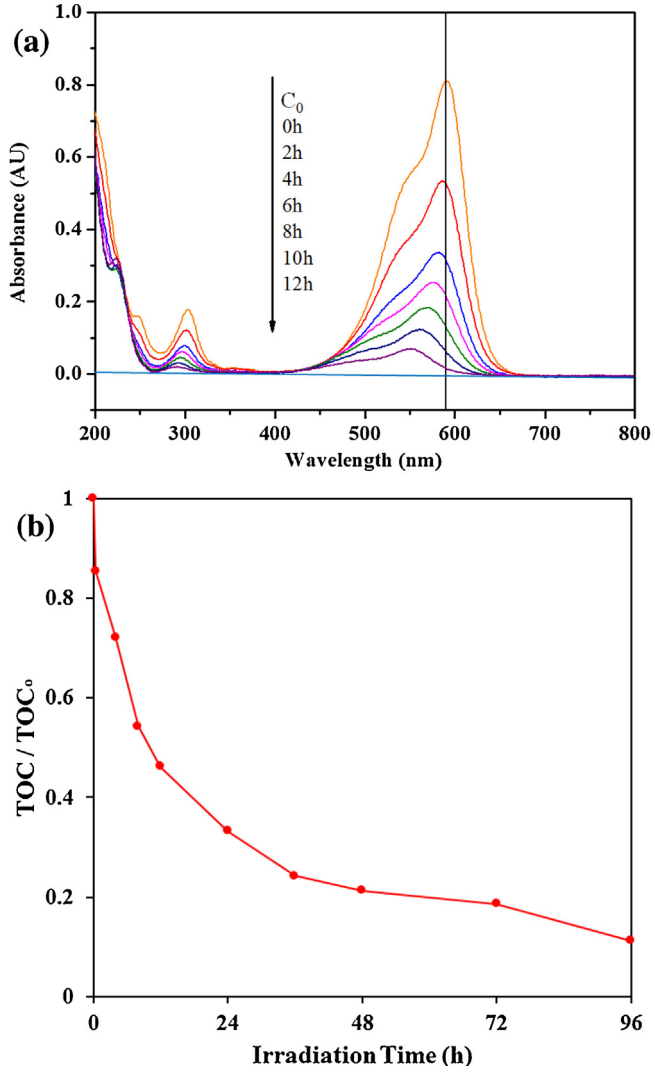

Fig. 7. (a) Temporal UV–vis adsorption spectral and (b) depletion of TOC change during the photocatalytic degradation of CV over aqueous photocatalyst under visible light irradiation. (10 mg/100 mL $PbBiO_2Br$/BiOBr, 10 ppm CV).

an effective photoexcited electron–hole separation and, consequently, enhance the photocatalytic activity. The driving force of charge transfer originates from the matching band potentials. Therefore, the suitable band potential is the precondition for the synergetic effect of heterojunction photocatalysts. Typically for $V_2O_5/BiVO_4$ heterostructured photocatalysts, [61] the conduction-band (CB) potential level of $BiVO_4$ is more negative than that of V_2O_5 so that photogenerated electrons could migrate from $BiVO_4$ to V_2O_5 driven by the contact electric field. Fig. 11 shows the type-I heterostructure band alignment [60] and the valence-band (VB) XPS spectra of $PbBiO_2Br$ and BiOBr. In the type-I band alignment, both VB and CB edges of $PbBiO_2Br$ are localized within the energy gap of BiOBr, forming the straddling band alignment (Fig. 11). The VB and CB potentials of two different semiconductors play a crucial role in the determination of the physical features of photogenerated charges and the photocatalytic performance. $PbBiO_2Br$/BiOBr heterostructured photocatalysts, the CB potential level of BiOBr, is more negative than that of $PbBiO_2Br$ so that photogenerated electrons could migrate from BiOBr to $PbBiO_2Br$ driven by the contact electric field. As the CB potentials of BiOBr (0.25 eV) and $PbBiO_2Br$ (0.48 eV) are a little different, the photoexcited electron is easy to transfer from the CB of BiOBr to the CB of $PbBiO_2Br$; and, the VB potentials of BiOBr (3.05 eV) and $PbBiO_2Br$ (2.88 eV) are also a little different that the photoexcited holes are easy to transfer from the VB of BiOBr to the VB of $PbBiO_2Br$. Therefore, $PbBiO_2Br$/BiOBr photocatalysts show great increase in the separation extent and lifetime of the photogenerated electrons, leading to the effective photodegradation of CV under visible light irradiation.

The generation of $O_2^{-\bullet}$ could not only inhibit the recombination of photoinduced charge carriers but also benefit the degradation of CV. The hydroxyl radical HO might be formatted by an $e^- \rightarrow O_2^{-\bullet} \rightarrow H_2O_2 \rightarrow {}^{\bullet}OH$ route and/or h^+ with OH^- and H_2O species [62]. On the basis of above reports, a proposed mechanism of degradation is illustrated in Fig. 11. Once the electron and the hole reach the CB and the VB of $PbBiO_2Br$, it induces the formation of active oxygen species, which cause the degradation of CV. It is clear that, except for the photodegradation of CV by the route of $PbBiO_2Br$/BiOBr-mediated and photosensitized processes, another type of photocatalytic route accounts for the enhanced photocatalytic activity. In Fig. 11, both the photosensitized and photocatalytic processes are preceded concurrently. However, in photosensitized and photocatalytic processes, O_2^- radicals are generated by the reaction of photogenerated and pho-

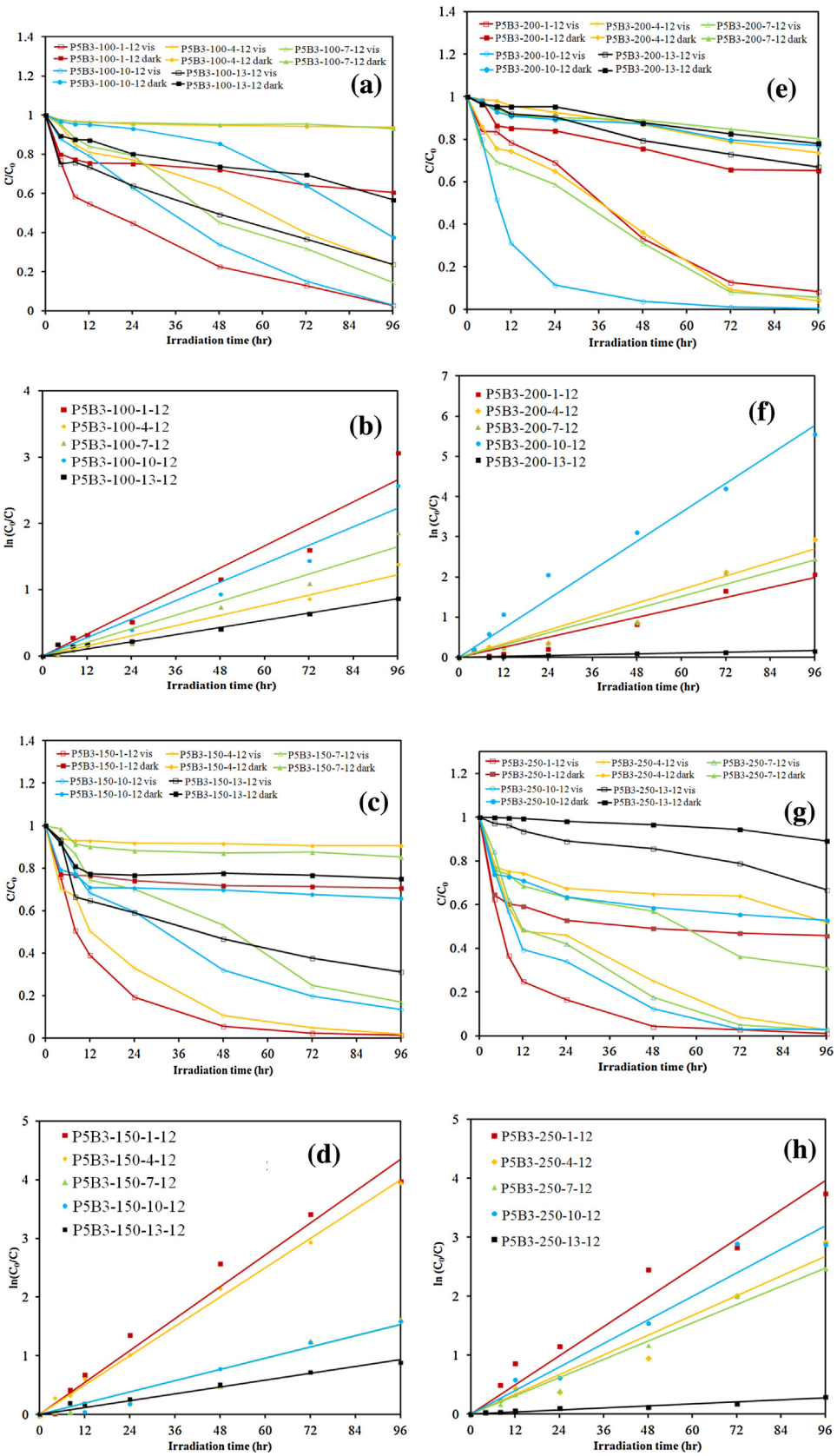

Fig. 8. Photocatalytic degradation of CV as a function of irradiation time over different photocatalysts. (Molar ratio $Pb(NO_3)_2/BiBr_3$ = 5/3, pH = 1–13, reaction temperature = 100–250 °C, reaction time 12 h).

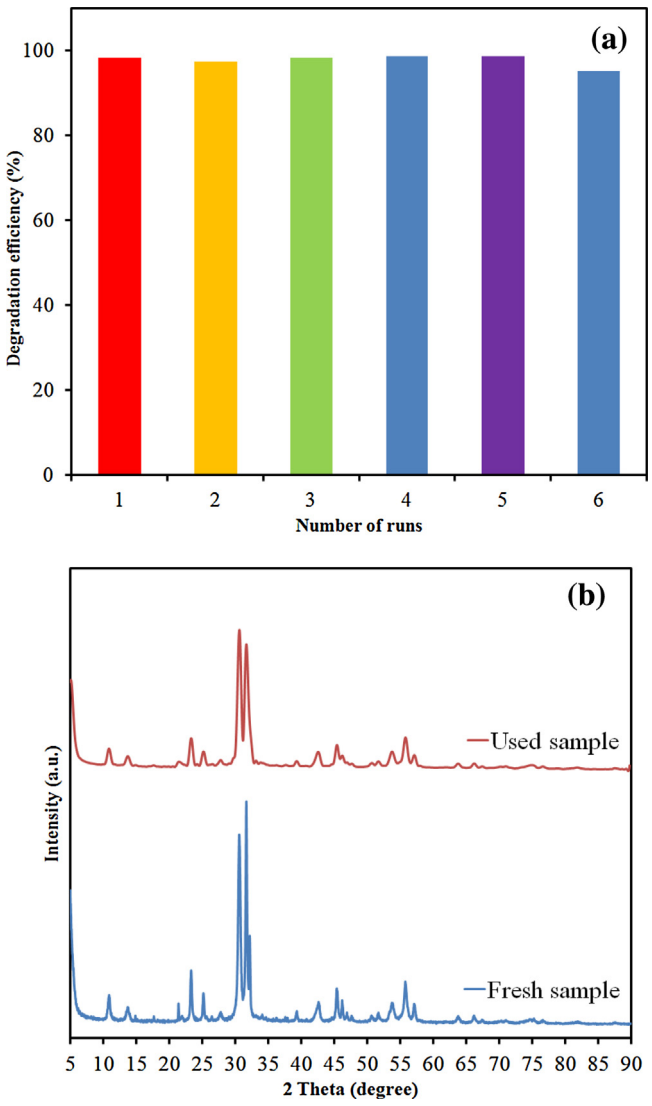

Fig. 9. (a) Cycling runs and (b) XRD patterns acquired before and after in the photocatalytic degradation of CV in the presence of P5B3-200-10-12 ($PbBiO_2Br$/BiOBr).

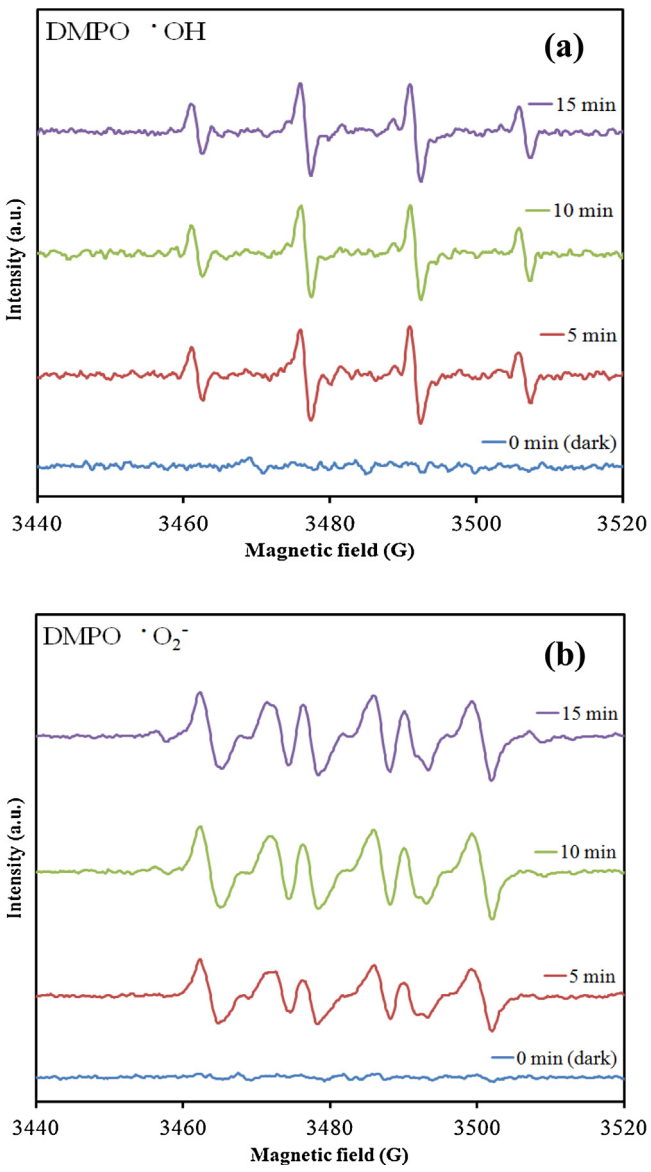

Fig. 10. DMPO spin-trapping EPR spectra for (a) DMPO-OH and (b) DMPO-O_2^- under visible light irradiation with P5B3-200-10-12 ($PbBiO_2Br$/BiOBr).

tosensitized electron with oxygen gas on the photocatalyst surface, and OH radicals are also generated by the reaction of O_2^- radicals with H^+ ion and hole h^+ with OH^- ion (or H_2O). These cycles continuously occur when the system is exposed to visible-light irradiation [55]; and, after several cycles of photo-oxidation, the degradation of CV by the produced oxidant species can be expressed by Eqs.9–10:

$$CV + O_2^{-\bullet}/OH^{\bullet} \rightarrow \text{degradedcompounds} \quad (9)$$

$$CV^{+\bullet} + O_2^{-\bullet}/OH^{\bullet} \rightarrow \text{degradedcompounds} \quad (10)$$

In a visible-light-induced semiconductor system, hydroxylated compounds were also identified for the photocatalytic degradation of CV [55,57]. In earlier reports [62,63], the *N*-dealkylation processes were preceded by the generation of a nitrogen-centered radical, and the destruction of the dye chromophore structure was preceded by the formation of a carbon-centered radical in the photocatalytic degradation of CV dye under UV or visible light irradiation. The reaction mechanisms for Bi_2SiO_5/g-C_3N_4-mediated photocatalytic processes proposed in this research should offer some notion for the applications to the decoloration of dyes.

4. Conclusions

The $PbBiO_2Br$/BiOBr heterojunctions have been synthesized by using template-free hydrothermal methods for the first time. The removal efficiency is significantly enhanced in the presence of $PbBiO_2Br$/BiOBr. The increased photocatalytic activities of $PbBiO_2Br$/BiOBr could be attributed to the formation of the heterojunction between $PbBiO_2Br$ and BiOBr, which effectively suppresses the recombination of photo-generated electron–hole pairs. It can be concluded that the enhanced photocatalytic activities of $PbBiO_2Br$/BiOBr materials could be owe to the formation of the heterojunction. The quenching effects and the EPR results illustrate that the reactive O_2^- plays the major and OH plays the minor role in the CV degradation. This work is useful for the synthesis of $PbBiO_2Br$/BiOBr and the photocatalytic degradation of CV at future applications to environmental pollution and control.

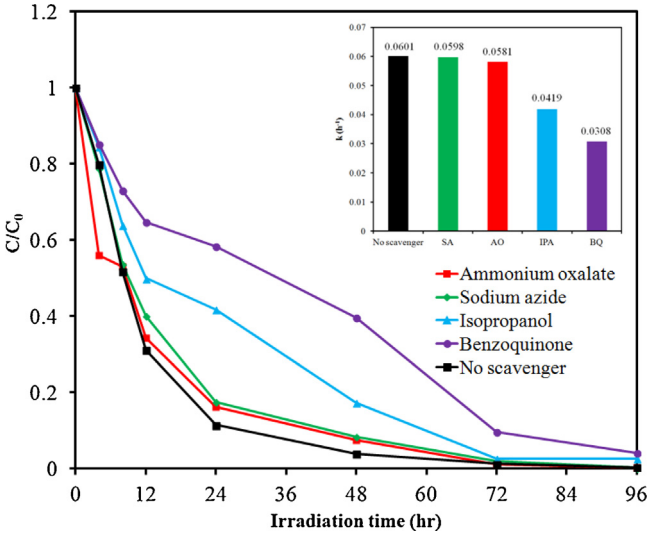

Fig. 11. The CV concentration during photodegradation as a function of irradiation time observed in P5B3-200-10-12 ($PbBiO_2Br$/BiOBr) under the addition of different scavengers: SA, IPA, AQ, and BQ.

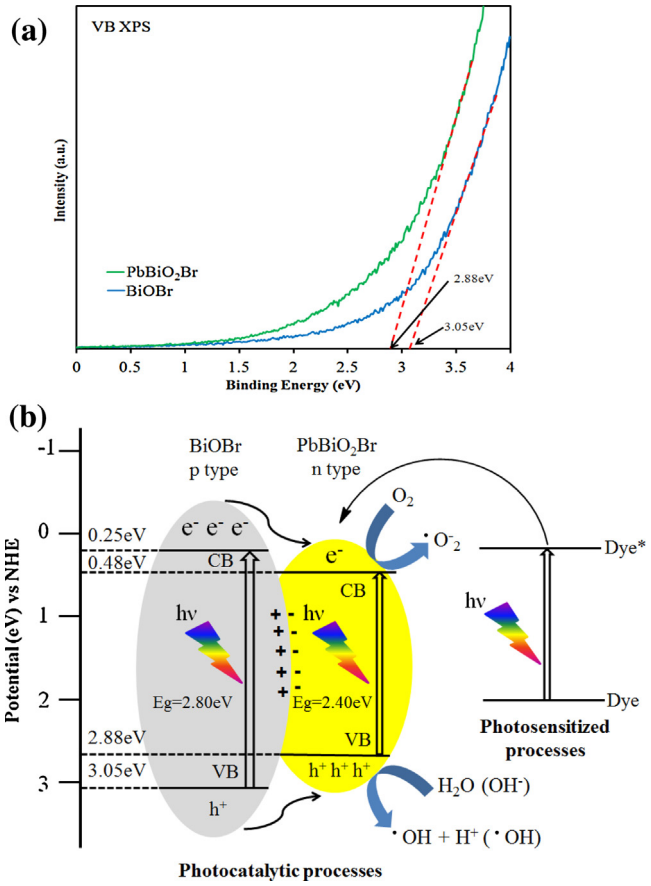

Fig. 12. (a) Valence band XPS of $PbBiO_2Br$ and BiOBr. (b) Schematic illustration of the band gap structures of P5B3-200-10-12 ($PbBiO_2Br$/BiOBr).

Acknowledgments

This research was supported by the Ministry of Science and Technology of the Republic of China (MOST-104-2113-M-142-001).

Appendix A. Supplementary data

Supplementary data associated with this article can be found, in the online version, at http://dx.doi.org/10.1016/j.molcata.2016.03.021.

References

[1] M.R. Hoffmann, S.T. Martin, W. Choi, D.W. Bahnemann, Chem. Rev. 95 (1995) 69–96.
[2] M. Urbani, M. Grätzel, M.K. Nazeeruddin, T. Torres, Chem. Rev. 114 (2014) 12330–12396.
[3] A. Kubacka, M. Fernández-García, G. Colón, Chem. Rev. 112 (2012) 1555–1614.
[4] D.F. Duxbury, Chem. Rev. 93 (1993) 381–433.
[5] B.P. Cho, T. Yang, L.R. Blankenship, J.D. Moody, M. Churchwell, F.A. Bebland, S.J. Culp, Chem. Res. Toxicol. 16 (2003) 285–294.
[6] H.P. Lin, C.C. Chen, W.W. Lee, Y.Y. Lai, J.Y. Chen, Y.Q. Chen, J.Y. Fu, RSC Adv. 6 (2016) 2323–2336.
[7] S.T. Huang, Y.R. Jiang, S.Y. Chou, Y.M. Dai, C.C. Chen, J. Mol. Catal. A: Chem. 391 (2014) 105–120.
[8] K. Yu, S. Yang, C. Liu, H. Chen, H. Li, C. Sun, S.A. Boyd, Environ. Sci. Technol. 46 (2012) 7318–7326.
[9] W.L.W. Lee, J.S. Lin, J.L. Chang, J.Y. Chen, M.C. Cheng, C.C. Chen, J. Mol. Catal. A: Chem. 361–362 (2012) 80–90.
[10] F. Chen, P. Fang, Y. Gao, Z. Liu, Y. Liu, Y. Dai, Chem. Eng. J. 204–206 (2012) 107–113.
[11] C. Lu, Y. Wu, F. Mai, W. Chung, C. Wu, W. Lin, C. Chen, J. Mol.Catal. A: Chem. 310 (2009) 159–165.
[12] S.T. Huang, C.S. Lu, J.L. Chang, W.S. Huang, C.C. Chen, J. Taiwan Inst. Chem. Eng. 45 (2014) 1927–1936.
[13] W.L.W. Lee, W.H. Chung, W.S. Huang, W.C. Lin, W.Y. Lin, Y.R. Jiang, C.C. Chen, J. Taiwan Inst. Chem. Eng. 44 (2013) 660–669.
[14] H.B. Lu, S. M.Wang, L. Zhao, J.C. Li, B.H. Dong, Z.X. Xua, J. Mater. Chem. 21 (2011) 4228–4234.
[15] M.A. El-Sayed, Acc. Chem. Res. 37 (2004) 326–333.
[16] H. Yu, J. Li, R.A. Loomis, P.C. Gibbons, Wang, W.E. Buhro, J. Am. Chem. Soc. 125 (2003) 16168–16169.
[17] H. Cheng, B. Huang, Y. Dai, Nanoscale 6 (2014) 2009–2026.
[18] L. Ye, J. Chen, L. Tian, J. Liu, T. Penga, K. Deng, L. Zan, Appl. Catal. B: Environ. 130–131 (2013) 1–7.
[19] Y.H. Liao, J.X. Wang, J.S. Lin, W.H. Chung, W.Y. Lin, C.C. Chen, Catal.Today 174 (2011) 148–159.
[20] J.A. Seabold, K.S. Choi, J. Am. Chem. Soc. 134 (2012) 2186–2192.
[21] Z. Chen, H. Jiang, W. Jin, C. Shi, Appl. Catal. B: Environ. 180 (2016) 698–706.
[22] W. Wei, Y. Dai, B.B. Huang, J. Phys. Chem. C 113 (2009) 5658–5663.
[23] M. Batuk, D. Batuk, A.A. Tsirlin, D.S. Filimonov, Chem. Mater. 27 (2015) 2946–2956.
[24] F.Y. Xiao, J. Xing, L. Wu, Z.P. Chen, X.L. Wang, H.G. Yang, RSC Adv. 3 (2013) 10687–10690.
[25] Y. Yu, Y. Gu, W. Zheng, Y. Ding, Y. Cao, J. Phys. Chem. C 119 (2015) 28190–28193.
[26] S. Fuldner, P. Pohla, H. Bartling, S. Dankesreiter, R. Stadler, M. Gruber, A. Pfitzner, B. Konig, Green Chem. 13 (2011) 640–643.
[27] Z. Shan, W. Wang, X. Lin, H. Ding, F. Huang, J. Solid State Chem. 181 (2008) 1361–1366.
[28] S. Rau, B. Schafer, D. Gleich, E. Anders, M. Rudolph, M. Friedrich, H. Gorls, W. Henry, J.G. Vos, Angew. Chem. 118 (2006) 6361–6364.
[29] A. Pfitzner, P. Pohla, Z. Anorg, Allg. Chem. 635 (2009) 1157–1159.
[30] H. Xie, C. Jia, Y. Jiang, X. Wang, Mater. Chem. Phys. 133 (2012) 1003–1005.
[31] C. He, M. Gu, Scripta Mater. 55 (2006) 481–484.
[32] J.D, Y. Liu, X. Pan, Y. Zhang, J. Yu, K. Nakajim, H. Taniguchi, Catal. Comm. 39 (2013) 65–69.
[33] X. Li, J. Wang, D. Xu, Z. Sun, Q. Zhao, W. Peng, Y. Li, G. Zhang, F. Zhang, X. Fan, ACS Sustainable Chem. Eng. 3 (2015) 1017–1022.
[34] P. Wang, B. Huang, X. Qin, X. Zhang, Y. Dai, J. Wei, M.H. Whangbo, Angew. Chem. Int. Ed. 47 (2008) 7931–7933.
[35] M.C. Yin, Z.S. Li, J.H. Kou, Z.G. Zou, Environ. Sci. Technol. 43 (2009) 8361–8366.
[36] L.S. Zhang, K.H. Wong, H.Y. Yip, C. Hu, J.C. Yu, C.Y. Chan, P.K. Wong, Environ. Sci. Technol. 44 (2010) 1392–1398.
[37] S.G. Meng, D.Z. Li, M. Sun, W.J. Li, J.X. Wang, J. Chen, X.Z. Fu, G.C. Xiao, Catal. Commun. 12 (2011) 972–975.
[38] G. Li, K.H. Wong, X. Zhang, C. Hu, J.C. Yu, R.C.Y. Chan, P.K. Wong, Chemosphere 76 (2009) 1185–1191.
[39] H.L. Chen, W.W. Lee, W.H. Chung, H.P. Lin, Y.J. Chen, Y.R. Jiang, W.Y. Lin, C.C. Chen, J. Taiwan Inst. Chem. Eng. 45 (2014) 1892–1909.
[40] M.M. Rahman, K.M. Krishna, T. Soga, T. Jimbo, M. Umeno, J. Phys. Chem. Solid 60 (1999) 201–210.
[41] A.I. Kovalev, D.L. Wainstein, A.Y. Rashkovskiy, A. Osherov, Y. Golan, Surf. Interface Anal. 42 (2010) 850–854.
[42] N.B. Rahna, V. Kalarivalappil, M. Nageri, S.C. Pillai, S.J. Hinder, V. Kumar, B.K. Vijayan, Mater. Sci. Semicon. Proc. 42 (2016) 303–310.
[43] Y.R. Jiang, H.P. Lin, W.H. Chung, Y.M. Dai, W.Y. Lin, C.C. Chen, J. Hazard. Mater. 283 (2015) 787–805.

[44] S.T. Huang, Y.R. Jiang, S.Y. Chou, Y.M. Dai, C.C. Chen, J. Mol. Catal. A: Chem. 391 (2014) 105–120.
[45] Y.R. Jiang, S.Y. Chou, J.L. Chang, S.T. Huang, H.P. Lin, C.C. Chen, RSC Adv. 5 (2015) 30851–30860.
[46] L. Lin, S. Yuan, J. Chen, L. Wang, J. Wan, X. Lu, Chemosphere 78 (2010) 66–71.
[47] F. Dong, Y. Sun, M. Fu, Z. Wu, S.C. Lee, J. Hazard. Mater. 219–220 (2012) 26–34.
[48] A. Chatzitakis, C. Berberidou, I. Paspaltsis, G. Kyriakou, T. Sklaviadis, I. Poulios. Water Res. 42 (2008) 386–394.
[49] C. Nasr, K. Vinodgopal, L. Fisher, S. Hotchandani, A.K. Chattopadhyay, P.V. Kamat, J. Phys. Chem. 100 (1996) 8436–8442.
[50] X. Xiao, R. Hao, M. Liang, X. Zuo, J. Nan, L. Li, W. Zhang, J. Hazard. Mater. 233–234 (2012) 122–130.
[51] N.M. Dimitrijevic, B.K. Vijayan, O.G. Poluektov, T. Rajh, K.A. Gray, H. He, P. Zapol, J. Am. Chem. Soc. 133 (2011) 3964–3971.
[52] J. Ma, C. Wang, H. He, Appl. Catal. B: Environ. 184 (2016) 28–34.
[53] W. Zou, L. Zhang, L. Liu, X. Wang, J. Sun, S. Wu, Y. Deng, C. Tang, F. Gao, L. Dong, App. Catal. B: Environ. 181 (2016) 495–503.
[54] D. Jiang, J. Li, C. Xing, Z. Zhang, S. Meng, M. Chen, ACS Appl. Mater. Interfaces 7 (2015) 19234–19242.
[55] Y. Tian, B. Chang, J. Lu, J. Fu, F. Xi, X. Dong, ACS Appl. Mater. Interfaces 5 (2013) 7079–7085.
[56] A.O. Kondrakov, A.N. Ignatev, V.V. Lunin, F.H. Frimmel, S. Bräse, H. Horn, Appl. Catal. B: Environ. 182 (2016) 424–430.
[57] W.W. Lee, C.S. Lu, C.W. Chuang, Y.J. Chen, J.Y. Fu, C.W. Siao, C.C. Chen, RSC Adv. 5 (2015) 23450–23463.
[58] X. Xiao, C. Xing, G. He, X. Zuo, J. Nan, L. Wang, Appl. Catal. B: Environ. 148–149 (2014) 154–163.
[59] H. Li, Y. Zhou, W. Tu, J. Ye, Z. Zou, Adv. Funct. Mater. 25 (2015) 998–1013.
[60] Z. Li, J. Feng, S. Yan, Z. Zou, Nano Today 10 (2015) 468–486.
[61] J. Su, X.X. Zou, G.D. Li, X. Wei, C. Yan, Y.N. Wang, J. Zhao, L.J. Zhou, J.S. Chen, J. Phys. Chem. C 115 (2011) 8064.
[62] H.J. Fan, C.S. Lu, W.L.W. Lee, M.R. Chiou, C.C. Chen, J. Hazard. Mater. 185 (2011) 227–235.
[63] S. Ameen, M.S. Akhtar, M. Nazim, H.S. Shin, Mater. Lett. 96 (2013) 228–232.